Invited Article: Complex vibrational susceptibility by interferometric Fourier transform stimulated Raman scattering

Vikas Kumar, Alejandro De la Cadena, Antonio Perri, Fabrizio Preda, Nicola Coluccelli, Giulio Cerullo, and Dario Polli

Citation: APL Photonics **3**, 092403 (2018); doi: 10.1063/1.5034114

View online: https://doi.org/10.1063/1.5034114

View Table of Contents: http://aip.scitation.org/toc/app/3/9

Published by the American Institute of Physics

Invited Article: Complex vibrational susceptibility by interferometric Fourier transform stimulated Raman scattering

Vikas Kumar, Alejandro De la Cadena, Antonio Perri, Fabrizio Preda, Nicola Coluccelli, Giulio Cerullo, and Dario Polli[a]
IFN-CNR and Dipartimento di Fisica, Politecnico di Milano, Piazza Leonardo da Vinci, 32, 20133 Milano, Italy

(Received 9 April 2018; accepted 29 May 2018; published online 26 July 2018)

We introduce interferometric (I) Fourier-transform (FT) stimulated Raman scattering (SRS) to measure the complex nonlinear vibrational susceptibility of molecules. The technique is a simple variation of FT-SRS, which was previously demonstrated to combine the very high sensitivity of single-channel lock-in detection with the spectral resolution afforded by FT spectroscopy. In IFT-SRS, a local oscillator, temporally anticipated with respect to the broadband pump pulse, enables the interferometric detection of both real and imaginary parts of the nonlinear susceptibility, whose spectrum is recorded in the time domain by scanning the delay of the local oscillator using a birefringent common-path interferometer. We apply IFT-SRS to record the complex vibrational response of different solvents and their mixtures.
https://doi.org/10.1063/1.5034114

Coherent Raman scattering (CRS) is a powerful label-free spectroscopic technique which allows fingerprinting of molecules based on their intrinsic vibrational response, finding a growing range of applications in biomedical optics and materials science.[1,2] CRS is a class of third-order nonlinear optical processes which make use of two frequency detuned light pulses, the pump (at frequency ω_{pu}) and the Stokes (at frequency ω_S), to drive a nonlinear polarization in the sample under investigation. In coherent anti-Stokes Raman scattering (CARS),[3] the nonlinear polarization is generated at the anti-Stokes frequency and radiates a field whose intensity is measured by using the detector. In stimulated Raman scattering (SRS),[4] the nonlinear polarization is generated at either the Stokes or the pump frequency and results in amplification/attenuation of their intensities, in a process known as stimulated Raman gain (SRG)/stimulated Raman loss (SRL).

The nonlinear polarization is proportional to the third-order nonlinear susceptibility $\chi^{(3)}(\omega) = \chi_R^{(3)}(\omega) + \chi_{NR}^{(3)}$, where $\chi_R^{(3)}(\omega)$ is the resonant susceptibility, typically described as the superposition of complex Lorentzian functions corresponding to the vibrational transitions of the molecules under study (damped, driven harmonic oscillators), and $\chi_{NR}^{(3)}$ is the real, frequency-independent non-resonant susceptibility generated by the electronic transitions of the molecules themselves and of the surrounding medium. Standard CRS techniques typically do not allow us to retrieve the full complex nonlinear susceptibility. In the CARS process, the signal is proportional to $|\chi_R^{(3)}(\omega) + \chi_{NR}^{(3)}|^2 = |\chi_R^{(3)}(\omega)|^2 + \chi_{NR}^{(3)2} + 2\chi_{NR}^{(3)}Re[\chi_R^{(3)}(\omega)]$, thus mixing real and imaginary parts of the nonlinear susceptibility, while in SRS, the signal is proportional to $\mathrm{Im}[\chi_R^{(3)}(\omega)]$, thus retrieving only the imaginary part. The complex susceptibility can in principle be retrieved using analytic techniques such as the maximum entropy method[5] or the Kramers-Kronig relation,[6] but such approaches require the full spectrum of the nonlinear susceptibility, which is often not available. Direct experimental access to the complex nonlinear susceptibility would allow richer spectroscopic information, especially in the presence of unknown mixtures of molecular species; in particular, the vibrational

[a]Author to whom correspondence should be addressed: dario.polli@polimi.it

phase may provide an additional contrast mechanism similar to the Zernike phase contrast mechanism in standard microscopy.[7]

The measurement of amplitude and phase of a light field typically requires interferometric approaches, in which the field is superimposed with a phase-coherent local oscillator (LO). In interferometric CARS (I-CARS), a LO field E_{LO} is generated at the anti-Stokes frequency and collinearly combined with the anti-Stokes field E_{aS} to give the signal[8]

$$I(\omega) \cong |E_{LO}|^2 + |E_{aS}|^2 + 2E_{LO}E_{pu}^2E_S\left\{\mathrm{Re}\left[\chi_R^{(3)}(\omega) + \chi_{NR}^{(3)}\right]\cos(\Phi) + \mathrm{Im}\left[\chi_R^{(3)}(\omega)\right]\sin(\Phi)\right\},$$

where $E_{pu}(E_S)$ is the pump (Stokes) field and Φ is the phase difference between the LO and the anti-Stokes field. By setting Φ to $\pi/2$ and 0, respectively, one can retrieve the pure real and imaginary parts of $\chi^{(3)}$ and thus the full complex nonlinear susceptibility. I-CARS is technically very demanding because of the requirement to superimpose and synchronize on the sample three light beams (pump, Stokes, and LO) and to maintain phase coherence between the CARS field and the LO. It was demonstrated using an auxiliary nonlinear medium to generate the LO signal[9] or exploiting the phase-preserving chain constituted by the pump, signal, and idler beams of an optical parametric oscillator (OPO).[10,11] I-CARS has been extensively used to retrieve the complex nonlinear susceptibility of molecules[12] and to perform vibrational phase imaging.[13] Alternatively, in single-beam CARS the vibrational phase can be retrieved by the use of spectral phase shaping of a broadband pulse in combination with double quadrature spectral interferometry.[14,15] Finally, vibrational phase imaging has been implemented in wide-field CARS without the requirement of a LO, by the use of a wave-front sensor to measure the phase of the anti-Stokes field[16,17] or by the acquisition of images at different longitudinal planes combined with an iterative phase retrieval algorithm.[18]

Recently, Robles *et al.* extended interferometric detection to SRS,[19,20] generating with a pulse shaper a time-anticipated replica of a broadband Stokes pulse, which is not temporally overlapped with the narrowband pump pulse and acts as LO; by measuring with an optical multichannel analyzer the spectral interference pattern of Stokes and LO in the presence and absence of the pump pulse, they retrieved the complex nonlinear susceptibility using standard spectral interferometry approaches.[21] They demonstrated that the spectral phase of the SRS signal is more robust, compared to the spectral amplitude, with respect to the noise induced by laser amplitude fluctuations. Despite the elegance of the approach, the use of a spectrometer as a detector limits the maximum modulation frequency of the pump pulse to a few tens of kHz (as limited by the readout speed of commercially available line cameras) and thus the sensitivity in detection of the SRS signal, which is typically maximized for a given integration time employing laser oscillators at multi-MHz repetition rates.

Recently, we introduced a novel technique for broadband SRS microscopy based on Fourier-transform (FT) detection of the SRS spectrum.[22] In FT-SRS, a linear interferometer, based on a passive birefringent delay line, is used to detect in the time domain the broad spectrum of the Stokes pulse. The linearity of the FT operator is further exploited to detect in the time domain also the SRG spectrum, by high-frequency modulation of the pump and synchronous detection with a single-channel lock-in amplifier. FT-SRS combines the sensitivity of single-channel lock-in detection with the spectral resolution allowed by FT spectroscopy. In this paper, we introduce a simple modification of the FT-SRS technique, which we call interferometric FT-SRS (IFT-SRS), allowing the retrieval of the full complex nonlinear susceptibility of the sample. In IFT-SRS, a reference LO beam is generated before the sample and is used for a full reconstruction of the nonlinear SRS signal by time-domain interferometry.

The conceptual scheme of IFT-SRS is shown in Fig. 1 for a configuration in which the SRL of a broadband pump pulse is detected, according to the so-called inverse Raman scattering;[23] very similar considerations hold for a broadband Stokes pulse and SRG detection. The pump pulse is first sent to a birefringent plate (BP) with a polarization at 45° with respect to its fast and slow axes, thus generating a LO pulse perpendicularly polarized with respect to the pump and anticipated by a few picoseconds. The pump and a narrowband Stokes pulse, modulated at high frequency, are collinearly superposed, synchronized, and focused on the sample. While the pump undergoes SRL through modulation transfer from the Stokes, the LO does not experience any nonlinear interaction

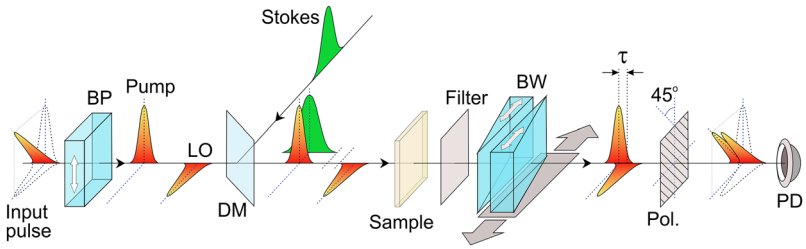

FIG. 1. Conceptual scheme of IFT-SRS. BP: birefringent plate; LO: local oscillator pulse; DM: dichroic mirror; BW: birefringent wedges; Pol: polarizer; PD: photodetector.

due to the lack of temporal overlap with the Stokes. After the sample, pump and LO are spectrally filtered from the Stokes and sent to a delay line, which consists of a pair of birefringent wedges (BW) with the optical axis rotated by 90° with respect to the BP. The BW allow us to vary the overall delay τ between the pump and the LO from zero to a few picoseconds. After the BW, the pump and LO are projected to a common polarization direction by using a linear polarizer and they interfere on a photodetector, whose output is sent to a lock-in amplifier which records both the linear interferogram $I(\tau)$ and the differential interferogram $\Delta I(\tau)$.

To understand the operation of IFT-SRS, let us consider the interference of the broadband pump beam, modulated by the SRS effect, with a LO delayed by τ. The interferogram can be expressed as the following Fourier integral:

$$I(\tau) = \int_{-\infty}^{+\infty} \left|\tilde{E}_{pu}(\omega) + \Delta\tilde{E}_{pu}(\omega) + \tilde{E}_{LO}(\omega)\exp(i\omega\tau)\right|^2 d\omega, \tag{1}$$

which, considering terms only up to the first order in $\Delta\tilde{E}_{pu}(\omega)$, becomes

$$\begin{aligned} I(\tau) \cong \int_{-\infty}^{+\infty} \Big(&\left|\tilde{E}_{pu}(\omega)\right|^2 + \left|\tilde{E}_{LO}(\omega)\right|^2 + 2\,\mathrm{Re}\Big(\tilde{E}_{pu}(\omega)\Delta\tilde{E}^*_{pu}(\omega) + \tilde{E}_{pu}(\omega)\tilde{E}^*_{LO}(\omega)\exp(-i\omega\tau) \\ &+ \Delta\tilde{E}_{pu}(\omega)\tilde{E}^*_{LO}(\omega)\exp(-i\omega\tau)\Big)\Big) d\omega. \end{aligned} \tag{2}$$

Lock-in detection only retains the modulated terms, and the differential interferogram thus becomes

$$\Delta I(\tau) \cong \int_{-\infty}^{+\infty} 2\,\mathrm{Re}\Big(\tilde{E}_{pu}(\omega)\Delta\tilde{E}^*_{pu}(\omega) + \Delta\tilde{E}_{pu}(\omega)\tilde{E}^*_{LO}(\omega)\exp(i\omega\tau)\Big) d\omega. \tag{3}$$

Now considering the SRS signal (SRL of the pump) as

$$\Delta\tilde{E}_{pu}(\omega) = -ib\chi^{(3)}(\omega)\left|\tilde{E}_S\right|^2\tilde{E}_{pu}(\omega) \tag{4}$$

and the LO as a fraction of the pump beam, $\tilde{E}_{LO}(\omega) = c\tilde{E}_{pu}(\omega)$, with b and c being two proportionality constants, the differential interferogram becomes

$$\begin{aligned} \Delta I(\tau) &= \Delta I_{CW} + \int_{-\infty}^{+\infty} 2bc\left|\tilde{E}_S\right|^2\left|\tilde{E}_{pu}(\omega)\right|^2\mathrm{Re}\Big(-ib\chi^{(3)}(\omega)\exp(i\omega\tau)\Big) d\omega \\ &= \Delta I_{CW} + \int_{-\infty}^{+\infty} 2bc\left|\tilde{E}_S\right|^2\left|\tilde{E}_{pu}(\omega)\right|^2\Big(\cos(\omega\tau)\mathrm{Im}\left[\chi^{(3)}(\omega)\right] - \sin(\omega\tau)\,\mathrm{Re}\left[\chi^{(3)}(\omega)\right]\Big) d\omega. \end{aligned} \tag{5}$$

In this formula, we have called ΔI_{CW} those terms that do not depend upon the delay τ; they only create a constant offset in the interferogram that disappears when computing the FT of $\Delta I(\tau)$, which we call $\Delta\tilde{I}(\omega)$. Therefore, one can write

$$\mathrm{Re}\left[\Delta\tilde{I}(\omega)\right] = +2bc\left|\tilde{E}_S\right|^2\left|\tilde{E}_{pu}(\omega)\right|^2\mathrm{Im}\left[\chi^{(3)}(\omega)\right], \tag{6a}$$

$$\mathrm{Im}\left[\Delta\tilde{I}(\omega)\right] = -2bc\left|\tilde{E}_S\right|^2\left|\tilde{E}_{pu}(\omega)\right|^2\mathrm{Re}\left[\chi^{(3)}(\omega)\right], \tag{6b}$$

showing that the FT of the differential interferogram allows retrieving simultaneously real and imaginary parts of the nonlinear susceptibility.

The experimental setup for IFT-SRS is shown in Fig. 2. The system starts with a commercial Yb: fiber laser system (Coherent Fidelity), generating 140 fs pulses at 1040 nm with 10 W average power and 80 MHz repetition rate. An etalon (SLS Optics) spectrally filters a 4 W fraction of

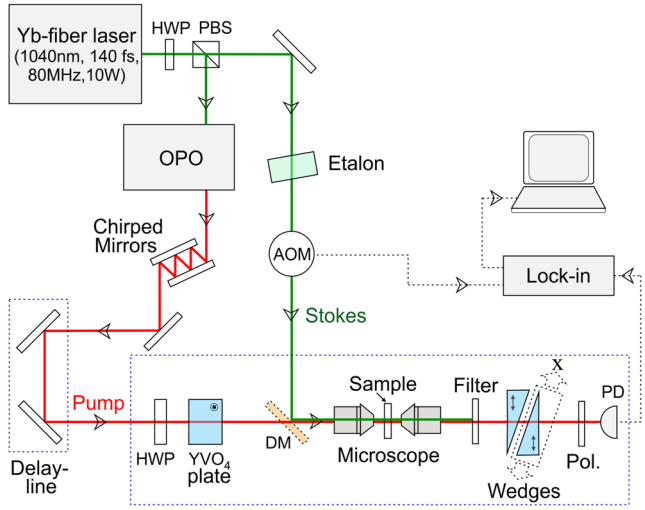

FIG. 2. Experimental setup for IFT-SRS. HWP: half-wave plate; PBS: polarizing beam splitter; AOM: acousto-optic modulator; DM: dichroic mirror; Pol.: polarizer; PD: photodetector.

the output, thus generating narrowband Stokes pulses with 700 mW average power and 15 cm^{-1} bandwidth. The Stokes pulses are further amplitude modulated at 1 MHz frequency by using an acousto-optic modulator (AOM, AA Opto-Electronic). For the SRS experiment, we employ the first-order diffracted Stokes beam with 140 mW average power, which is fully modulated. The zeroth-order un-diffracted AOM output is sent to a photodiode to generate the reference signal for lock-in detection. The remainder of the laser output drives a home-made OPO, specially designed to provide broadband 30 fs pulses[24] with up to 500 mW average power, employed as the broadband pump beam in the SRS process. For these experiments, we tuned the OPO spectrum to span the 780-815 nm range [see Fig. 3(c)], corresponding to a 2700-3200 cm^{-1} frequency detuning with respect to the 1040 nm light, thus covering the whole C—H stretching region of molecules. The pump beam (with 75 mW average power) is compressed by a double-bounce reflection on a pair of chirped mirrors, sent to a delay line for synchronization and then to a 6 mm-thick YVO_4 BP with the vertical optical axis, which produces the LO pulse anticipated by 4.84 ps. Before the BP, a half-wave plate rotates the polarization of the pump beam by approximately 45°; a fine adjustment of its rotation allows us to precisely control the pump/LO relative intensities. Pump and Stokes beams are then collinearly combined by using a dichroic mirror and focused on the sample by using a microscope objective with a 0.3 numerical aperture. Average power levels on the sample were kept at approx. 10 mW for the broadband beam (i.e., 5 mW for the pump and 5 mW for the LO) and 30-35 mW for the modulated Stokes beam. The transmitted pump and the LO, collimated by using an identical objective and filtered from the Stokes by a series of short-pass filters, are sent to a pair of YVO_4 BW with the optical axis rotated by 90° with respect to the BP. The BW introduce a delay of opposite sign with respect to the BP, resulting in an overall delay tunable between −3.2 and +3.2 ps. For our measurement, we typically perform asymmetric scans in the −0.4 to +2 ps range, which matches the spectral resolution determined by the bandwidth of the Stokes pulse. The orthogonally polarized pump and LO are projected to a common polarization by using a linear polarizer and interfere on a silicon photodiode (Thorlabs, PDA36A-EC). Its output is sent to a lock-in amplifier (Zurich Instruments, HF2LI), both to its analog-to-digital converter port with the input bandwidth limited to 20 kHz, to record the linear interferogram, and to its high-frequency demodulator port, to record the differential interferogram. Both the interferograms are recorded simultaneously as a function of the BW insertion x, and the corresponding delay τ is obtained by a calibration procedure,[25] which consists of measuring the interferograms of the pump field filtered by a series of narrow bandpass filters. The quality of the calibration is further verified by measuring the SRS spectrum of a known compound.

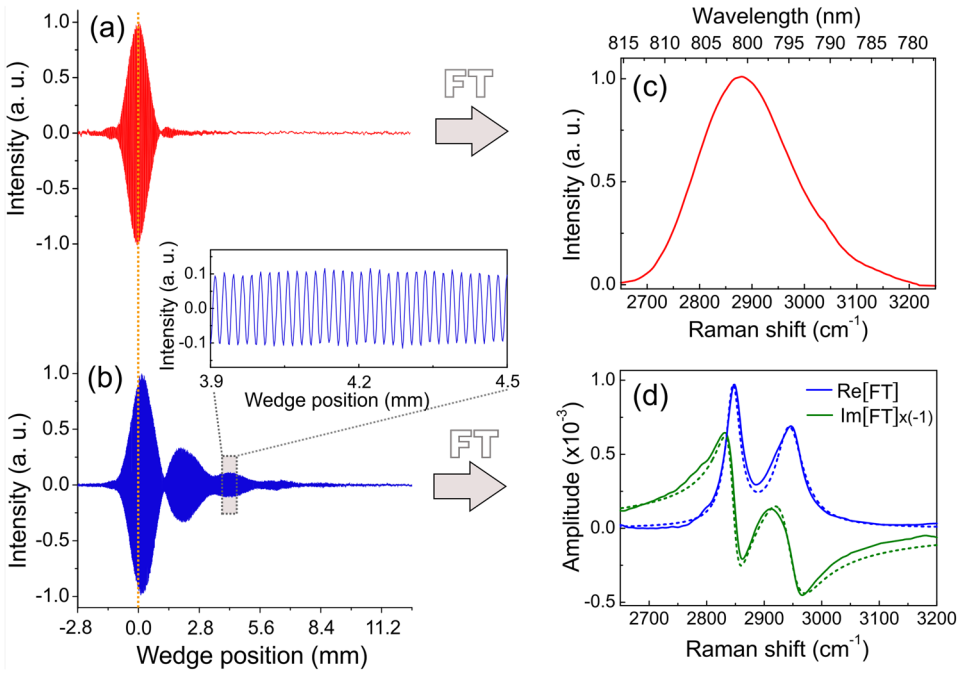

FIG. 3. IFT-SRS of methanol. (a) Linear interferogram; (b) differential interferogram; (c) FT of the linear interferogram; (d) solid lines: real (blue) and imaginary (green) parts of the FT of the differential interferogram; dashed lines: fits according to Eq. (7), with $\Omega_1 = 2840\ \text{cm}^{-1}$, $\Gamma_1 = 15\ \text{cm}^{-1}$, $\Omega_2 = 2945\ \text{cm}^{-1}$, and $\Gamma_2 = 28\ \text{cm}^{-1}$. Note that the horizontal scale of the interferograms in panels (a) and (b) is the position of the moving wedge x (as sketched in Fig. 2) and corresponds to a delay that is frequency-dependent;[25] however, due to the limited bandwidth of the pump, this can be well approximated with the first-order term in the series expansion, equal to $\approx 7\ \mu$m/fs. This corresponds to a delay between the two replicas that varies from −0.4 to +1.8 ps in panels (a) and (b).

Figure 3 shows IFT-SRS measurements performed on pure methanol contained in a cuvette with 1 mm path length. Panel (a) displays the linear interferogram of the pump and LO pulses, which is nearly symmetric (small asymmetries are attributed to polarization dependent transmission along the beam path). Panel (b) reports the differential interferogram that is, as expected, strongly asymmetric since the nonlinear interaction "drills" holes in the pump pulse spectrum, which in the time domain correspond to field oscillations on the trailing edge (positive values of the delays) of the pulse. The absence of oscillations on the leading edge (negative values of the delays) is dictated by the causality principle: at time zero, the pump and Stokes pulses interact with the sample and, in the presence of a resonance condition (i.e., when the difference between their photon energies matches a vibrational transition of the molecule), a vibrational coherence is set in the sample that oscillates in time *after* the interaction occurred and decays on the picosecond time scale, as expected for Raman signals in the liquid phase.[26] Figure 3(c) shows the FT of the linear interferogram, which corresponds to the pump pulse spectrum. Finally, Fig. 3(d) reports the FT of the differential interferogram. In accordance to Eq. (6a), the real part of the FT provides the imaginary part of $\chi^{(3)}$ and displays an absorptive line shape with two peaks at 2840 and 2945 cm^{-1}, corresponding to the symmetric and antisymmetric CH_3 stretching modes of methanol. Analogously, as dictated by Eq. (6b), the imaginary part of the FT corresponds to the real part of $\chi^{(3)}$ and shows a clear dispersive behavior, with two inflection points corresponding to the two vibrational peaks. The spectra were fitted with a sum of complex Lorentzian functions of the kind

$$\chi^{(3)}(\omega) = \sum\nolimits_k \frac{A_k}{\omega - \Omega_k - i\Gamma_k}, \tag{7}$$

where Ω_k are the resonance frequencies and Γ_k are the linewidths of the vibrational transitions. The fits, shown in Fig. 3(d) as dashed lines, are in excellent agreement with the experimental results.

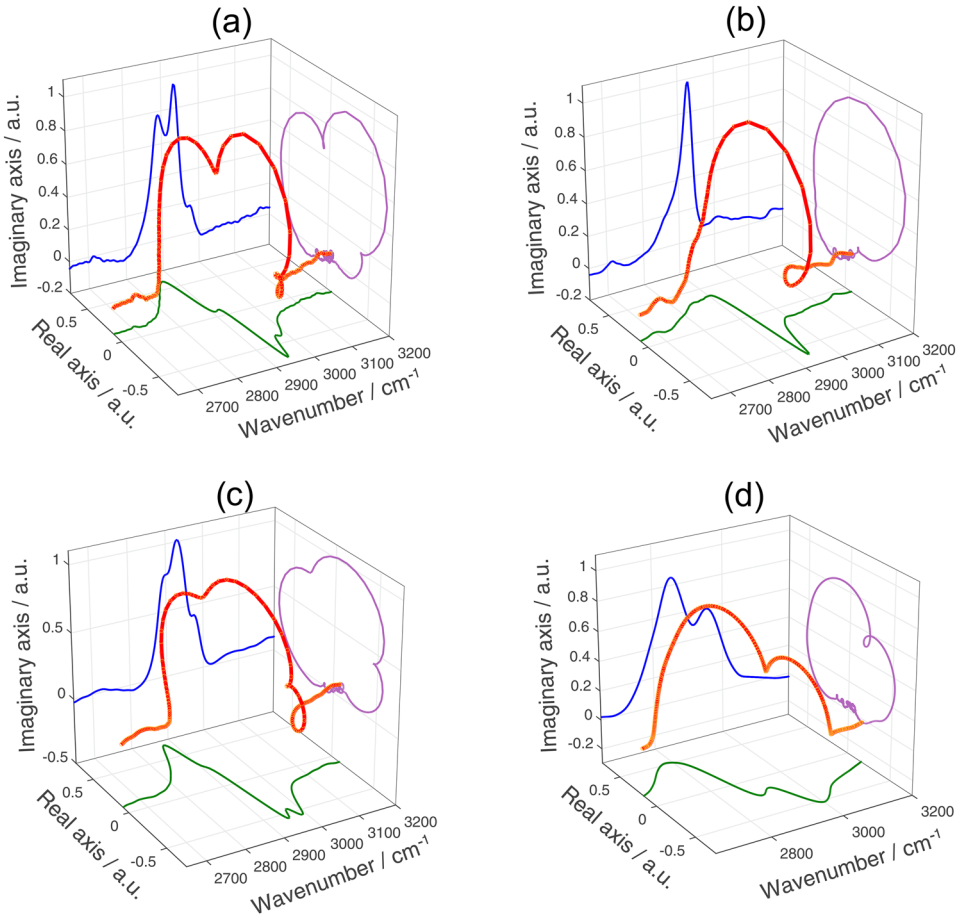

FIG. 4. IFT-SRS spectra of different solvents: (a) ethanol, (b) acetone, (c) isopropanol, and (d) tetrahydrofuran (THF).

Figure 4 shows IFT-SRS spectra of different solvents, such as ethanol, acetone, isopropanol, and tetrahydrofuran (THF). In this case, we employed a "roller coaster" three-dimensional representation of the signal (red curve): for every vibrational frequency (horizontal axis labeled "wavenumber"), the IFT-SRS signal has a real (horizontal axis) and an imaginary (vertical axis) component. The projection of this three-dimensional curve on the vertical plane (imaginary axis versus vibrational frequency) provides the absorptive Raman response (blue curve), which is similar to the spontaneous Raman spectrum. All the solvents in Fig. 4 show well-resolved spectra in this vertical plane, in good agreement with the tabulated spontaneous Raman spectra of the solvents. The projection on the floor/horizontal plane (real axis versus vibrational frequency) provides the dispersive-like Raman response (green curve).

Of great interest is also the projection onto the complex plane (purple curve, imaginary axis versus real axis). For every vibrational frequency, the complex Raman signal has an amplitude and phase that can be represented as a point in this complex plane, defined by a vector length and angle. A single isolated resonance (corresponding to a purely Lorentzian complex function) traces a circle in the complex plane as a function of frequency, as we can see for the case of acetone [displaying a single dominating peak at 2922 cm^{-1} in the region of interest, see Fig. 4(b)]. Multiple resonances result in additional loops: it is the case for THF [two vibrational modes and two loops in the complex plane, see Fig. 4(d)] and ethanol/isopropanol [three vibrational modes and three loops in the complex plane, see Figs. 4(a) and 4(c)].

The benefit of the complex plane plot is most evident when two or more chemical species with overlapping vibrational spectra are present, such as the case of methanol, ethanol, and their mixture (Fig. 5). As one can see, both the real dispersive-like part of the $\chi_R^{(3)}(\omega)$ [Fig. 5(c)] and its imaginary

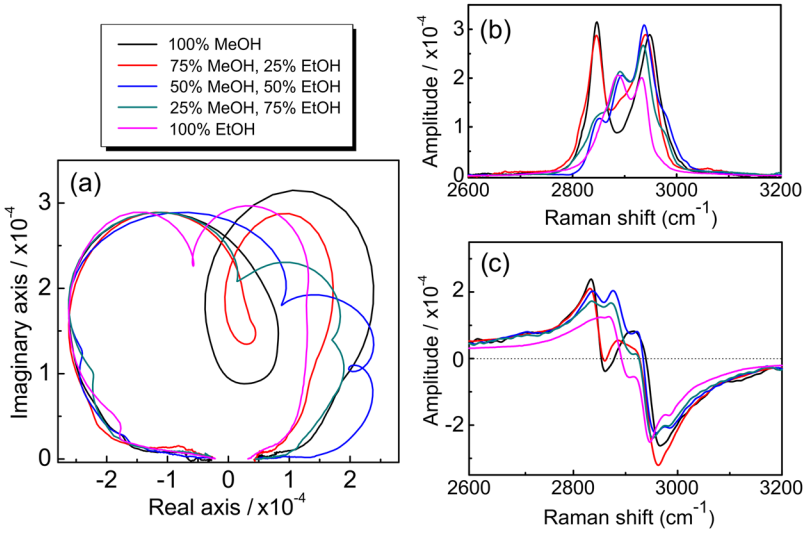

FIG. 5. Complex SRS response of mixtures of methanol and ethanol in different ratios as indicated. (a) Projection of the signal in the complex plane: starting from zero signal out of resonance and walking through the Raman response toward increasing wavenumbers, the spirals are drawn in an anti-clockwise manner. [(b) and (c)] The signals represented in the imaginary (b) and real (c) planes. To highlight similarities and differences in the plots for different mixtures, we normalized the imaginary/real axes in panel (a) by the maxima/minima values near 2945 cm^{-1} Raman resonance of the 100% methanol curves in panel (a)/panel (b).

part with absorptive line shape [Fig. 5(b)] display very similar profiles so that it is hard to distinguish the various concentrations. On the other hand, the phase plots [Fig. 5(a)] show very distinctive features, with a variable number and position of the loops in the spirals. Availability of the complex response thus increases the achievable chemical selectivity and sensitivity of CRS techniques. We note that care should be taken in extending this technique to thick inhomogeneous samples in the presence of birefringence. In such a case, the polarizations of the beams could undergo a slight rotation that could result in a variation of the absolute values of the real and imaginary parts of the nonlinear vibrational susceptibility.

In conclusion, we have presented here a simple modification to our previously introduced FT-SRS technique, which does not increase its experimental complexity. Using a thick birefringent plate before the sample, it is possible to generate a LO that enables the interferometric detection of both the real and imaginary components of the resonant susceptibility $\chi_R^{(3)}(\omega)$ over a broad spectral region. Being a FT spectroscopic technique, our approach bears no limitations in the bandwidth so that having at disposal a sufficiently broad pump (or Stokes) pulse one could access both the low-wavenumber "fingerprint" and the high-wavenumber "C—H stretching" regions of the vibrational spectrum of molecules, thus obtaining the most detailed information on the sample. The access to the real (dispersive) part of the Raman response provides precious extra information that is neither accessible with standard CRS techniques nor with standard spontaneous Raman scattering. In this way, quantitative characterization of mixtures can be made even when two or more components display similar amplitudes.

We acknowledge funding from the European Research Council under the Consolidator Grant VIBRA (ERC-2014-CoG No. 648615) and the Proof of Concept Grant CHIMERA (ERC-2016-POC No. 754802) and from the King Abdullah University of Science and Technology (KAUST, Project No. OSR-2016-CRG5-3017-01).

[1] J.-X. Cheng and X. S. Xie, *Coherent Raman Scattering Microscopy* (CRC Press, Boca Raton, FL, 2013).
[2] J.-X. Cheng and X. S. Xie, Science **350**, aaa8870 (2015).
[3] A. Zumbusch, G. R. Holtom, and X. S. Xie, Phys. Rev. Lett. **82**, 4142 (1999).
[4] C. W. Freudiger, W. Min, B. G. Saar, S. Lu, G. R. Holtom, C. He, J. C. Tsai, J. X. Kang, and X. S. Xie, Science **322**, 1857 (2008).
[5] E. M. Vartiainen, H. A. Rinia, M. Müller, and M. Bonn, Opt. Express **14**, 3622 (2006).

[6] Y. Liu, Y. J. Lee, and M. T. Cicerone, Opt. Lett. **34**, 1363 (2009).
[7] F. Zernike, Physica **9**, 686 (1942).
[8] C. L. Evans, E. O. Potma, and X. S. Xie, Opt. Lett. **29**, 2923 (2004).
[9] E. O. Potma, C. L. Evans, and X. S. Xie, Opt. Lett. **31**, 241 (2006).
[10] M. Jurna, J. P. Korterik, C. Otto, and H. L. Offerhaus, Opt. Express **15**, 15207 (2007).
[11] M. Jurna, J. P. Korterik, C. Otto, J. L. Herek, and H. L. Offerhaus, Opt. Express **16**, 15863 (2008).
[12] M. Jurna, J. P. Korterik, C. Otto, J. L. Herek, and H. L. Offerhaus, Phys. Rev. Lett. **103**, 043905 (2009).
[13] M. Jurna, E. T. Garbacik, J. P. Korterik, J. L. Herek, C. Otto, and H. L. Offerhaus, Anal. Chem. **82**, 7656 (2010).
[14] S.-H. Lim, A. G. Caster, and S. R. Leone, Phys. Rev. A **72**, 041803(R) (2005).
[15] A. Wipfler, J. Rehbinder, T. Buckup, and M. Motzkus, Opt. Lett. **37**, 4239 (2012).
[16] P. Berto, D. Gachet, P. Bon, S. Monneret, and H. Rigneault, "Wide-field vibrational phase imaging," Phys. Rev. Lett. **109**, 093902 (2012).
[17] P. Berto, A. Jesacher, C. Roider, S. Monneret, H. Rigneault, and M. Ritsch-Marte, Opt. Lett. **38**, 709–711 (2013).
[18] J. Zheng, D. Akimov, S. Heuke, M. Schmitt, B. Yao, T. Ye, M. Lei, P. Gao, and J. Popp, Opt. Express **23**, 10756 (2015).
[19] F. E. Robles, M. C. Fischer, and W. S. Warren, Opt. Express **24**, 485 (2016).
[20] F. E. Robles, K. C. Zhou, M. C. Fischer, and W. S. Warren, Optica **4**, 243 (2017).
[21] L. Lepetit, G. Chériaux, and M. Joffre, J. Opt. Soc. Am. B **12**, 2467 (1995).
[22] J. Réhault, F. Crisafi, V. Kumar, G. Ciardi, M. Marangoni, G. Cerullo, and D. Polli, Opt. Express **23**, 25235 (2015).
[23] W. J. Jones and B. P. Stoicheff, Phys. Rev. Lett. **13**, 657 (1964).
[24] N. Coluccelli, D. Viola, V. Kumar, A. Perri, M. Marangoni, G. Cerullo, and D. Polli, Opt. Lett. **42**, 4545 (2017).
[25] A. Perri, F. Preda, C. D'Andrea, E. Thyrhaug, G. Cerullo, D. Polli, and J. Hauer, Opt. Express **25**, A483 (2017).
[26] J. P. Ogilvie, E. Beaurepaire, A. Alexandrou, and M. Joffre, Opt. Lett. **31**, 480–482 (2006).